RESEARCH ARTICLE

ADVANCED THEORY AND SIMULATIONS
www.advtheorysimul.com

Non-Monotonic Variation of the Low Lattice Thermal Conductivity with Temperature in Penta-HgO_2 Sheet

*Asghar Hussain, Chenxin Zhang, Changsheng Hou, and Qian Wang**

Inspired by the experimental synthesis of bulk HgO_2 with the potential of exfoliation to form a penta-HgO_2 sheet composed entirely of pentagonal motifs, a detailed theoretical study on the lattice thermal conductivity by using first-principles calculations combined with the unified theory of thermal transport is performed. It is found that the penta-HgO_2 sheet is semiconducting with an indirect bandgap of 1.18 eV and possesses a low lattice thermal conductivity of 2.07 W m^{-1} K^{-1} (3.28 W m^{-1} K^{-1}) along the x (y)-direction at 300 K. More interestingly, the variation of its thermal conductivity with temperature is non-monotonic, different from most cases. The phonon dispersion, phonon scattering, and phonon coherence is further systematically investigated to understand the underlying physics. This results suggest that the strong intrinsic anharmonicity resulting from its unique atomic configuration with the buckled structure and the heavy element of Hg leads to a high scattering rate, resulting in the ultralow particle-like thermal transport of 0.20 W m^{-1} K^{-1} (0.01 W m^{-1} K^{-1}) in the x (y)-direction, while the narrow average frequency interval and strong phonon linewidth are responsible for the dominant coherent thermal transport and non-monotonic variation of the low lattice thermal conductivity of the penta-HgO_2 sheet.

1. Introduction

A family of more than 170 pentagon-based two-dimensional (2D) materials with distinct physical properties and a wide range of possible applications has been reported[1] since the theoretical prediction of penta-graphene.[2] For instance, ferromagnetism and antiferromagnetism have been found in penta-MnN_2,[3] penta-CoS_2,[4] penta-BN_2,[5,6] penta-ZnO_2,[7] and penta-$PdSe_2$.[8,9] Penta-PdS_2 was reported to possess ferroelasticity,[10] and piezoelectric responses have been found in some ternary pentagonal monolayers.[11,12] These theoretical advances have significantly stimulated experimental efforts in synthesizing such pentagon-based materials. Consequently, several pentagon-based materials have been synthesized using different methods. For example, penta-silicene nano-ribbon was synthesized through physical vapor deposition,[13] and penta-$PdSe_2$,[14] has been prepared in different ways, including mechanical exfoliation,[15,16] molecular beam epitaxy,[17] and chemical vapor deposition. Penta-NiN_2 was successfully synthesized under high pressure.[18] These breakthroughs have accelerated the research of properties and applications of pentagon-based materials.

Among the explored properties of 2D pentagon-based materials, thermal transport properties are of particular interest as pentagonal materials usually have complicated geometric structures, low symmetry, and polymorphic bonding features characterized by 3- and 4-foldcoordination, leading to strong phonon scattering and low lattice thermal conductivity. For instance, it was reported that the penta-Sb_2C sheet has an ultralow lattice thermal conductivity of 0.72 W m^{-1} K^{-1} at room temperature.[19] 2D penta-$PtTe_2$,[20] penta-$PdTe_2$,[21] penta-OsP_2,[22] and penta-RhS_2,[22] have been found to possess low thermal conductivities of 1.77, 1.42, 3.19, and 2.90 W m^{-1} K^{-1}, respectively. However, in the reported studies, phonon coherence transport (wave-like tunnelling)[23–26] has not yet been explored, which plays an important role in penta-sheets because of their strong anharmonicity.

Recently, Hou et al.[27] predicted new penta-sheets (MO_2, M = Zn, Cd, Hg) and studied the second harmonic generation response of penta-CdO_2 due to its non-centrosymmetricity. Additionally, Chen et al.[28] comprehensively studied the catalytic properties of the penta-HgO_2 sheet, which shows high catalytic activity with low Gibbs free energy for hydrogen evolution reaction. It was found that the penta-HgO_2 sheet is a promising candidate for high-performance photocatalytic water-splitting due to its suitable band alignments, ultrahigh anisotropic carrier mobility, excellent optical absorption properties, and high catalytic activity. However, the thermal transport properties of penta-HgO_2 remain unexplored. It can be expected that the penta-HgO_2 sheet possesses a low lattice thermal conductivity because of its complex pentagonal configuration and the heavy element Hg, which motivates us to carry out this study. In this work, we studied the thermal transport properties of penta-HgO_2 based on the unified theory of thermal transport by considering both particle-like phonon propagation and wave-like phonon tunnelling.

A. Hussain, C. Zhang, C. Hou, Q. Wang
School of Materials Science and Engineering
Peking University
Beijing 100871, China
E-mail: qianwang2@pku.edu.cn

DOI: 10.1002/adts.202400598

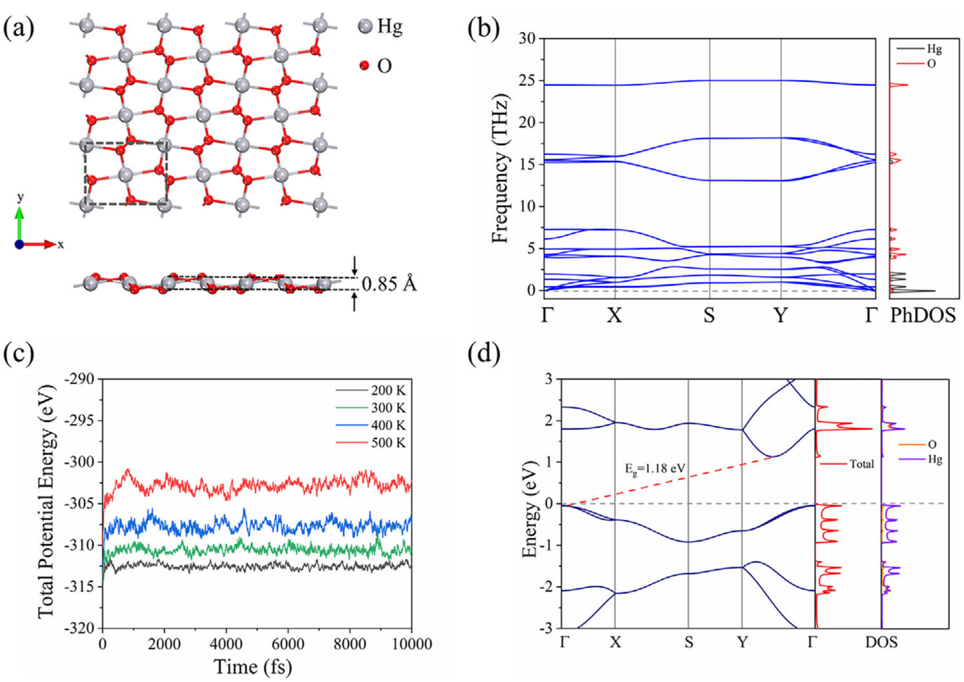

Figure 1. a) Top and side views, and b) phonon spectrum and PhDOS of the penta-HgO_2 sheet. c) Total potential energy fluctuation of the penta-HgO_2 sheet with time during the AIMD simulation at different temperatures. d) Electronic band structure and total and partial density of states (DOS) of the penta-HgO_2 sheet.

2. Results and Discussion

2.1. Geometric Structure, Stability, and Electronic Properties

The top and side views of the fully optimized penta-HgO_2 sheet are plotted in **Figure** 1a, showing a buckling of 0.85 Å. It has a penta-$PdSe_2$-like configuration[16] with *P-21/C* (No.14) symmetry and 6 atoms per unit cell. The unit cell of the penta-HgO_2 sheet has the lattice constants of $a = 4.47$ Å and $b = 6.31$ Å, including four oxygen atoms with Wyckoff position of 4e (0.52, 0.05, 0.41) and two mercury atoms with Wyckoff position of 2b (0.50, 0.00, 0.00). According to the Slack's rule,[29] the complicated geometric structure with heavy Hg atoms and low symmetry in penta-HgO_2 make it a potential candidate for a low thermal conductivity material.

To check the energetic stability of the competing β, γ, and α phases, we calculated their corresponding formation energy (E_{form}) defined as $E_{\text{form}} = (E_{\text{HgO2}} - nE_{\text{Hg}} - mE_{\text{O}}) / (n+m)$, here E_{HgO2} and $E_{\text{Hg}}/E_{\text{O}}$ are the energies of the penta-HgO_2 sheet and a free Hg/O atom, and n and m are the numbers of Hg and O atoms in the unit cell, respectively. Our calculated results show that the β phase with the space symmetry *P-21/C* is energetically most favorable with the formation energy of – 0.72 eV/atom, while that of the γ and α phases is – 0.68 and – 0.66 eV/atom, respectively. The atomic configurations of β, γ, and α phases are given in Figure S1 in the Supporting Information. We first calculated the phonon spectrum and the corresponding phonon density of states (PhDOS) for penta-HgO_2. As shown in Figure 1b, the absence of imaginary modes throughout the entire Brillouin zone confirms the dynamical stability of the penta-HgO_2 sheet. According to the PhDOS, Hg vibrations predominantly contribute to the acoustic phonon and low-frequency optical modes. In contrast, the high-frequency optical phonon modes mainly originate from O vibrations. This phenomenon is attributed to the mass difference between Hg and O atoms. Notably, the monoclinic symmetry exhibited in the penta-HgO_2 sheet is unique among binary pentagon-based sheets, which is distinct from the previously reported systems with monoclinic symmetry, such as penta-silicene,[30] and some ternary pentagon-based sheets like penta-FeAsS,[31] and penta-BCN.[11]

Next, we calculated the elastic constants C_{ij} (i, j = 1, 2, 6) using the finite distortion method [32] to study the mechanical stability and mechanical properties of the penta-HgO_2 sheet. As a monoclinic 2D material, all C_{ij} components of the penta-HgO_2 sheet possess nonzero and independent values: $C_{11} = 10.06$, $C_{22} = 67.09$, $C_{66} = 0.12$, $C_{12} = 7.58$, $C_{16} = 0.38$, and $C_{26} = 0.26$ N m^{-1}. It is noteworthy that all eigenvalues of the stiffness tensor matrix are positive, satisfying the Born-Huang criteria and indicating the mechanical stability of the penta-HgO_2 sheet. Additional detailed deductions can be found in the Supporting Information. To confirm the thermal stability of the penta-HgO_2 sheet, we also performed the ab initio molecular dynamics (AIMD) simulation for 10 *ps* from 200 to 500 K. Figure 1c shows the total potential energy without significant fluctuations up to 500 K. Our results suggest that the penta-HgO_2 sheet is not only thermally stable at room temperature and can withstand high temperatures up to 500 K.

We then investigated the electronic band structure of penta-HgO_2 to assess the feasibility of analyzing its thermal transport properties based on phonon contributions. As shown in Figure 1d, the penta-HgO_2 sheet exhibits semiconducting characteristics with an indirect band gap of 1.18 eV. By examining

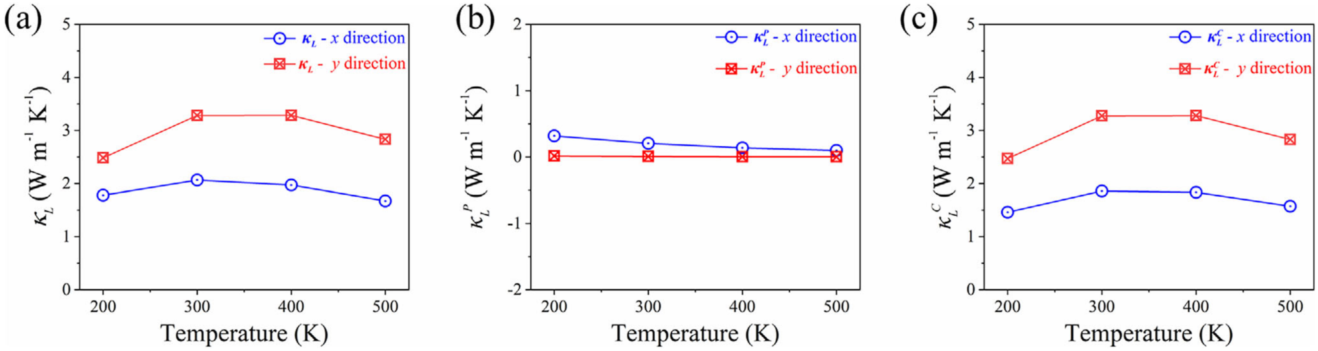

Figure 2. a) Total lattice thermal conductivity (κ_L), b) particle-like (κ_L^P), and c) phonon coherence (κ_L^C) contribution of the penta-HgO_2 sheet at different temperatures.

the corresponding total and partial density of states (DOS), we found that the O atoms mainly contribute to the electronic states in the valence band near the Fermi level, while the electronic states in the conduction bands originate from both Hg and O atoms. Since the penta-HgO_2 sheet is semiconducting, phonon transport dominates its thermal conductivity. Therefore, we study the lattice thermal conductivity of this sheet based on the unified framework of thermal transport,[23] namely considering the contributions to lattice thermal conductivity from phonon scattering and phonon coherence.

2.2. Lattice Thermal Conductivity from Particle-Like Contribution

Based on the unified theory of thermal transport, we calculated the thermal conductivity of the penta-HgO_2 sheet at room temperature. The setting of ShengBTE parameters is explained in the computational methods. As shown in **Figure** 2a, the maximum value of the thermal conductivity of penta-HgO_2 is 2.07 W m^{-1} K^{-1} along the x-direction and 3.28 W m^{-1} K^{-1} along the y-direction at 300 K, which is relatively low as compared to that of penta-OsP_2 (14.46 W m^{-1} K^{-1}) and penta-RhS_2 (3.20 W m^{-1} K^{-1}),[22] showing anisotropy of lattice thermal conductivity in these two directions, which can be understood from the different bonding features in the x and y directions as indicated in Figure S2 in Supporting Information. Also, in Table 1, we compare the lattice thermal conductivity of penta-HgO_2 with some other penta-sheets. The low κ_L in penta-HgO_2 can be attributed to the high atomic mass of Hg as well as the large Hg-O mass difference, which induces strong lattice anharmonicity in this system. This high atomic mass difference behavior is also similar to that of the experimentally studied BAs system.[33] In addition, as illustrated by Figure 2b, the particle-like contributions (κ_L^P) at 300 K are 0.20 W m^{-1} K^{-1} in the x-direction and 0.01 W m^{-1} K^{-1} in the y-direction, respectively. These results indicate that the intrinsic phonon particle-like contribution within the penta-HgO_2 sheet is very weak. To understand the origination of the ultralow particle-like contributions to lattice thermal conductivity, we further studied the phonon group velocity and high-order phonon scattering processes of penta-HgO_2.

Table 1. Comparison of the thermal conductivity (κ_L) of the penta-HgO_2 sheet with that of some other pentagonal sheets at room temperature.

Penta-Sheet	κ_L [W m^{-1} K^{-1}]	Reference
Penta-HgO_2	2.07 – 3.28	This work
Penta-graphene	645.00	[34]
Penta-$PtAs_2$	3.60	[1]
Penta-PtPTe	9.00	[35]

The calculated results of the three- and four-phonon scattering rates are plotted in **Figure** 3a, showing that both the three- and four-phonon scattering rates are strong at low phonon frequencies ranging from 0 to 7.50 THz. With the increase in phonon frequency, one can observe that both the three-phonon and four-phonon scattering rates display a decreasing trend. Due to the contribution of the low-frequency acoustic modes, which dominate most of the lattice thermal conductivity, higher scattering rates in the low-frequency region can suppress the particle-like contributions to the lattice thermal conductivity (see Figure S3, Supporting Information). Moreover, as shown in Figure 3b, penta-HgO_2 possesses a low group velocity. More precisely, the maximum group velocity is only 5.23 km s^{-1}, much less than that of penta-graphene (17.17 km s^{-1})[34] and penta-NiN_2 (10.97 km s^{-1}).[36] These findings indicate that the large size of Hg makes the Hg-O bond weaker than the C-C and Ni-N bonds. This not only results in the low group velocity but also leads to a high scattering rate, resulting in the ultralow κ_L^P.

2.3. Coherence Contribution to the Lattice Thermal Conductivity

The coherence contribution of phonons (κ_L^C) computed for the penta-HgO_2 sheet at different temperatures are plotted in Figure 2c. The maximum value κ_L^C along the x-direction is 1.85 W m^{-1} K^{-1}, and that for the y-direction is 3.27 W m^{-1} K^{-1}, significantly contributing to the κ_L due to the strong intrinsic phonon coherence. Phonons have a significant impact because their coherence contributions are 99.7% along the y-direction and 89.8% along the x-direction. Figure 2b and c collectively show that the total lattice thermal conductivity is dominated by κ_L^C, even at a relatively low temperature of 300 K.

As shown in Figure 2a and c, the non-monotonic variation of the penta-HgO_2 sheet is dominated by thermal transport within the material influenced by phonon coherence. According to the unified theory, phonon coherence contributions primarily

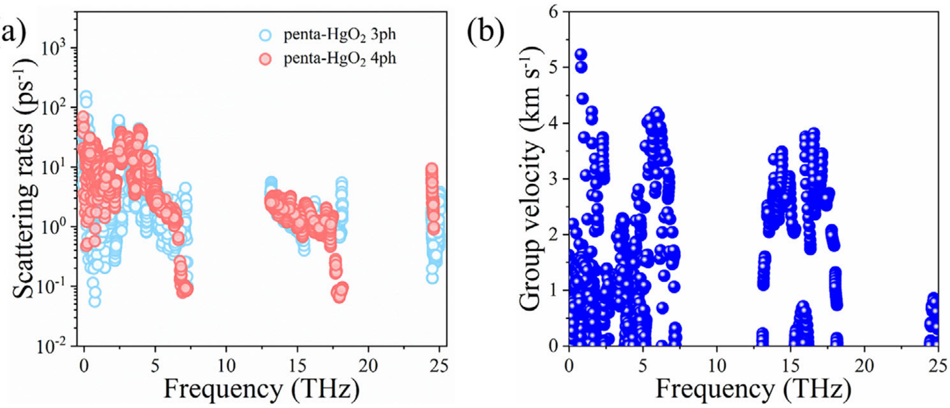

Figure 3. a) Phonon scattering rates of three- and four-phonon contributions at 300 K, and b) group velocity of the penta-HgO$_2$ sheet.

depend on the phonon scattering rates and phonon frequency intervals ($\Delta\omega(q)_{ij}$). According to the phonon dispersion plotted in Figure 1b, one can see some overlaps and closely spaced acoustic-optical bands (< 7.50 THz), leading to an ultralow average frequency interval between phonons. Contributed by the strong intrinsic anharmonicity and narrow frequency intervals of phonon modes, the lattice thermal conductivity contributed from κ_L^C is dominant within the whole temperature range.

To determine the exact contributions of coherent phonon modes in different frequency regions, we examine two mode-dependent contributions to the coherence thermal conductivity κ_L^C of the penta-HgO$_2$ sheet, which can quantify the coupling of two distinct phonon frequencies. **Figure** 4a–c show the contributions of degenerate and non-degenerate eigenstates in different temperature ranges. One can see that the contributions from the non-degenerate modes ($\omega_1 \neq \omega_2$) are dominant, whereas the contributions from the degenerate modes ($\omega_1 = \omega_2$) to κ_L^C are much less, as marked by the red dashed lines. The eigenstates with non-degenerate energy levels have sufficient scattering rates, resulting in their dominance in κ_L^C and exhibiting

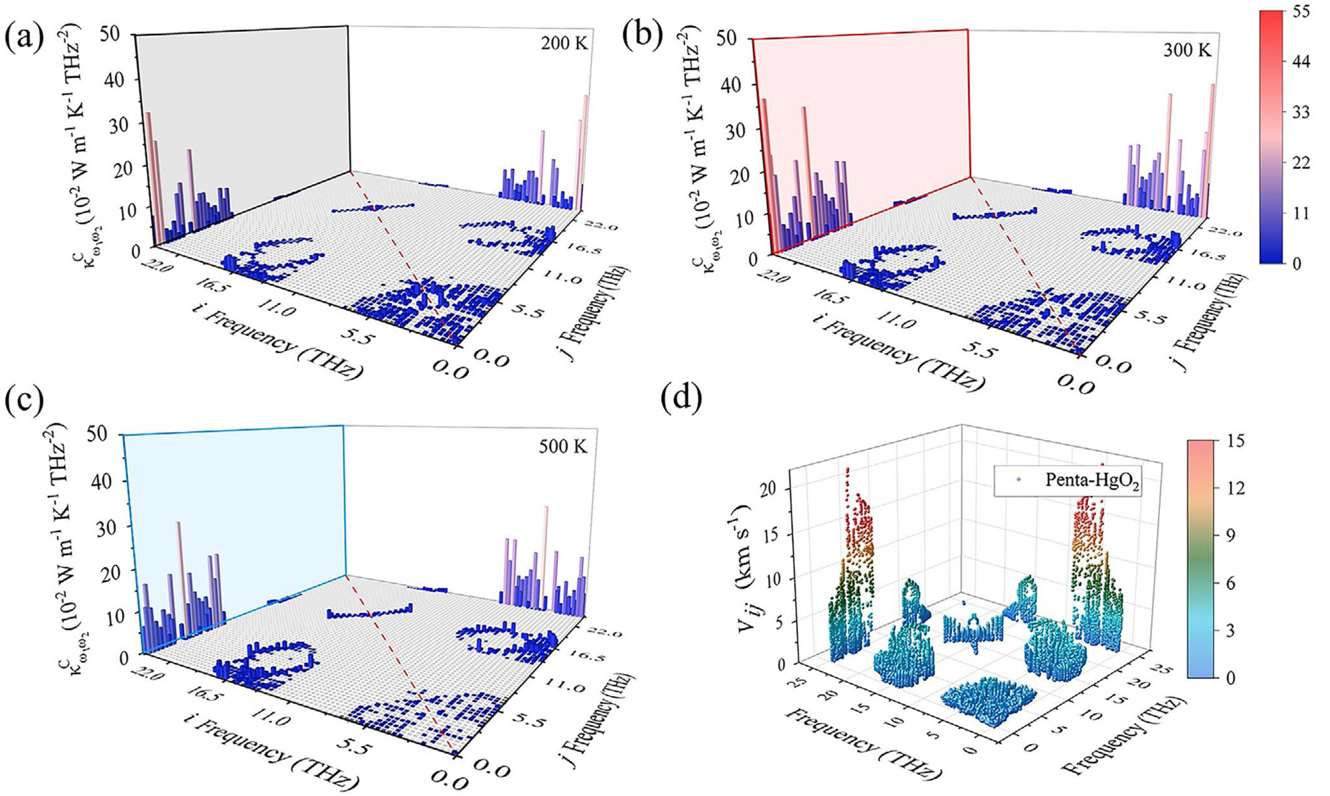

Figure 4. a–c) Two-mode-dependent contributions to κ_L^C versus the coupling phonon frequencies ω_1 and ω_2 with the degenerate modes presented by the dashed red lines, and d) generalized group velocity (V_{ij}) as a function of the frequency of the penta-HgO$_2$ sheet. The color map represents the absolute value of the generalized group velocity in km s^{-1}, with blue indicating lower velocities and red indicating higher velocities.

wave-like thermal transport. In addition, to better contrast the transport capabilities of phonon particle-like propagation and coherence, we plot the generalized group velocity (V_{ij}) of penta-HgO_2 as presented in Figure 4d. One can observe that coherent modes in the high-frequency range exhibit stronger coherent transport capabilities, with the generalized group velocity being higher than the corresponding group velocity in most frequency regions. This observation suggests that phonons have stronger thermal transport capability under coherent mechanism, increasing with the frequency of the phonon modes. Despite the high generalized group velocity indicating effective thermal transport, the thermal conductivity is greatly influenced by scattering rates, which increase rapidly with temperature (see Figure S4, Supporting Information). According to Equation (4), the lifetimes of the non-degenerate phonon modes have exhibited a non-monotonic change with the increase of scattering rates, which results in the contributions from the highest optical modes coupled with the low-frequency phonons showing a non-monotonic temperature dependence, as marked by the colored planes in Figure 4a–c. Additionally, excessively low lifetime results in a very low contribution of the degenerate modes to coherent thermal transport from 200 to 500 K. In a nutshell, based on the analysis of the contributions from the degenerate and non-degenerate eigenstates across different temperature ranges, the microscopic mechanism of the non-monotonic temperature dependence of lattice thermal conductivity in this strongly anharmonic penta-HgO_2 is elucidated.

3. Conclusion

In summary, by employing the higher-order phonon scattering theory and the unified theory of thermal transport, we investigated the thermal transport properties of the penta-HgO_2 sheet. Our calculations reveal that the lattice thermal conductivity is only 2.07 W m^{-1} K^{-1} along the x-direction and 3.28 W m^{-1} K^{-1} along the y-direction. More importantly, the phonon coherence thermal conductivity κ_L^C exhibits a dominant contribution from the non-degenerate modes, leading to a non-monotonic trend with temperature, while the contribution from the degenerate eigenstates to κ_L^C is much less sensitive to temperature. We elucidated the microscopic mechanism behind the non-monotonic phonon coherence contribution by a detailed analysis of the intricate three- and four-phonon scattering processes and the two-channel transport within this complicated pentagon-based structure. The methodologies employed in this study can be extended to explore other penta-sheets, particularly those synthesized experimentally, and can further provide new insights into understanding phonon coherence in monolayer penta-sheets.

4. Computational Methods

Our first-principle calculations have been carried out within the framework of density functional theory (DFT) implemented in the Vienna ab initio simulation package (VASP) package,[37] where the interactions between the ion cores and valence electrons are treated with the projector-augmented wave (PAW) method.[38,39] The Perdew-Burke-Ernzerhof functional (PBE)[40] within the generalized gradient approximation (GGA)[41] is employed for the exchange-correlation interaction among the electrons. The kinetic energy cut-off is set to 520 eV for the wave function. A 13×13×1 k-point grid used for the geometrical optimization. The values for the convergence criteria for the energy and force are set to 10^{-8} eV and 10^{-6} eV/Å, respectively. A vacuum space of 20.00 Å is included perpendicular to the penta-HgO_2 sheet to avoid interactions with its periodic images.

The total lattice thermal conductivity κ_L contains two components, particle-like (κ_L^P) and coherence (κ_L^C) contributions, as described in the unified theory of thermal transport.[42,43]

$$\kappa_L = \kappa_L^P + \kappa_L^C \tag{1}$$

The κ_L^P can be determined from the Boltzmann transport equation[44] in the framework of three-phonon and four-phonon scattering as follows:

$$\kappa_L^{P,\alpha\beta} = \frac{1}{k_B T^2 \Omega N} \sum_{\mathbf{q}} \sum_i \bar{N}(\mathbf{q})_i (\bar{N}(\mathbf{q})_i + 1)(\hbar\omega(\mathbf{q})_i)^2 V^\alpha(\mathbf{q})_i V^\beta(\mathbf{q})_i \tau(\mathbf{q})_i \tag{2}$$

Here, α and β represent the Cartesian coordinates of the coordinate system, and k_B , T, Ω, N, and $\hbar$ are the Boltzmann constant, the absolute temperature, volume of the unit cell, number of discrete $\mathbf{q}$ points in the Brillouin zone, and the reduced Plank constant, respectively. In addition, $\omega(\mathbf{q})_i$ and $\bar{N}(\mathbf{q})_i$ are the angular frequencies and the equilibrium Bose-Einstein distribution, indexed by wave vector $\mathbf{q}$ with the branch i, respectively. $V(\mathbf{q})_i$ is the phonon group velocity and $\tau(\mathbf{q})_i$ is the phonon lifetime.

The κ_L^P is calculated through the ShengBTE package[45] where the harmonic (second order) and anharmonic (third and fourth order) interatomic force constants (IFCs) are the inputs. For the penta-HgO_2 sheet, the phonon spectrum is obtained from PHONOPY[46] using the finite displacement method with a 3×3×1 supercell and 3×3×1 k-point mesh. The structures for calculating the third and fourth-order IFCs are generated using the Monte-Carlo random displacement method executed in the HIPHIVE package.[47] The cut-off distance is set to 9.50 Å for the second-order IFCs, while for the third and fourth-order IFCs, cut-off distances of 6.00 Å and 5.00 Å are applied, respectively. The thickness of the vacuum space for the calculations of lattice thermal conductivity is set to 4.25 Å, which is obtained by considering the buckling of this sheet and the van der Waals radius.[48,49] The convergent $\mathbf{q}$-mesh for ShengBTE calculations are set as 27×27×1 and 15×15×1 for third- and higher-order calculations (see Figure S5 for details, Supporting Information).

The phonon coherence contribution (κ_L^C) is calculated from the phonon coherence equation and lifetime matrix.[50]

$$\kappa_L^{C,\alpha\beta} = \frac{\hbar^2}{k_B T^2 \Omega N} \sum_{\mathbf{q}} \sum_{i\neq j} \frac{\omega(\mathbf{q})_i + \omega(\mathbf{q})_j}{2} V^\alpha(\mathbf{q})_{ij} V^\beta(\mathbf{q})_{ji} \times \frac{\omega(\mathbf{q})_i \bar{N}(\mathbf{q})_i (\bar{N}(\mathbf{q})_i + 1) + \omega(\mathbf{q})_j \bar{N}(\mathbf{q})_j (\bar{N}(\mathbf{q})_j + 1)}{4(\omega(\mathbf{q})_i - \omega(\mathbf{q})_j)^2 + (\Gamma(\mathbf{q})_i + \Gamma(\mathbf{q})_j)^2} \times (\Gamma(\mathbf{q})_i + \Gamma(\mathbf{q})_j) \tag{3}$$

$$\tau(\mathbf{q})_{ij} = \frac{2(\Gamma(\mathbf{q})_i + \Gamma(\mathbf{q})_j)}{4(\omega(\mathbf{q})_i - \omega(\mathbf{q})_j)^2 + (\Gamma(\mathbf{q})_i + \Gamma(\mathbf{q})_j)^2} \tag{4}$$

Where $\Gamma(\mathbf{q})_i = 1/\tau(\mathbf{q})_i$ is the phonon linewidth (scattering rate) of each phonon mode. The calculations for κ_L^C are computed using our in-house codes.

Supporting Information

Supporting Information is available from the Wiley Online Library or from the author.

Acknowledgements

This work was partially supported by grants from the National Natural Science Foundation of China (Grant No. NSFC-12274007), and was also supported by the High-Performance Computing Platform of Peking University, China.

Conflict of Interest

The authors declare no conflict of interest.

Data Availability Statement

The data that support the findings of this study are available from the corresponding author upon reasonable request.

Keywords

anharmonicity, lattice thermal conductivity, penta-HgO_2 sheet, phonon scattering, phonon coherence

Received: June 21, 2024
Revised: August 15, 2024
Published online: September 9, 2024

---

[1] Y. Shen, Q. Wang, *Phys. Rep.* **2022**, *964*, 1.
[2] S. Zhang, J. Zhou, Q. Wang, X. Chen, Y. Kawazoe, P. Jena, *Proc. Natl. Acad. Sci.* **2015**, *112*, 2372.
[3] K. Zhao, Q. Wang, *Appl. Surf. Sci.* **2020**, *505*, 144620.
[4] L. Liu, I. Kankam, H. L. Zhuang, *Phys. Rev. B* **2018**, *98*, 205425.
[5] M. Yagmurcukardes, H. Sahin, J. Kang, E. Torun, F. M. Peeters, R. T. Senger, *J. Appl. Phys.* **2015**, *118*, 104303.
[6] J. Li, X. Fan, Y. Wei, G. Chen, *Sci. Rep.* **2016**, *6*, 3184.
[7] L.-S. Zhao, Y. Wang, C.-P. Chen, L.-L. Liu, H.-X. Yu, Y. Zhang, Y. Chen, X.-C. Wang, *Phys. E: Low-Dimens. Syst. Nanostruct.* **2017**, *91*, 82.
[8] G. Liu, Q. Zeng, P. Zhu, R. Quhe, P. Lu, *Comput. Mat. Sci.* **2019**, *160*, 309.
[9] C. Long, Y. Liang, H. Jin, B. Huang, Y. Dai, *ACS Appl. Ener. Mater.* **2018**, *2*, 513.
[10] W. Zhang, Y. Cui, C. Zhu, B. Huang, S. Yan, *Phys. Chem. Chem. Phys.* **2021**, *23*, 10551.
[11] K. Zhao, Y. Guo, Y. Shen, Q. Wang, Y. Kawazoe, P. Jena, *J. Phys. Chem. Lett.* **2020**, *11*, 3501.
[12] T. Thanasarnsurapong, K. Dabsamut, T. Maluangnont, S. Jungthawan, A. Boonchun, *J. Appl. Phys.* **2021**, *129*, 095101.
[13] J. I. Cerdá, J. Sławińska, G. L.e Lay, A. C. Marele, J. M. Gómez-Rodríguez, M. E. Dávila, *Nat. Commun.* **2016**, *7*, 13076.
[14] X. Zhang, G. Su, J. Lu, W. Yang, W. Zhuang, K. Han, X. Wang, Y. Wan, X. Yu, P. Yang, *ACS Appl. Mater. Interfaces* **2021**, *13*, 43063.
[15] W. L. Chow, P. Yu, F. Liu, J. Hong, X. Wang, Q. Zeng, C. H. Hsu, C. Zhu, J. Zhou, X. Wang, *Adv. Mater.* **2017**, *29*, 1602969.
[16] A. D. Oyedele, S. Yang, L. Liang, A. A. Puretzky, K. Wang, J. Zhang, P. Yu, P. R. Pudasaini, A. W. Ghosh, Z. Liu, *J. Am. Chem. Soc.* **2017**, *139*, 14090.
[17] E. Li, D. Wang, P. Fan, R. Zhang, Y.-Y. Zhang, G. Li, J. Mao, Y. Wang, X. Lin, S. Du, *Nano Res.* **2018**, *11*, 5858.
[18] M. Bykov, E. Bykova, A. V. Ponomareva, F. Tasnadi, S. Chariton, V. B. Prakapenka, K. Glazyrin, J. S. Smith, M. F. Mahmood, I. A. Abrikosov, *ACS Nano* **2021**, *15*, 13539.
[19] X. Liu, T. Ouyang, D. Zhang, H. Huang, H. Wang, H. Wang, Y. Ni, *J. Appl. Phys.* **2020**, *127*, 205106.
[20] W.-L. Tao, Y.-Q. Zhao, Z.-Y. Zeng, X.-R. Chen, H.-Y. Geng, *ACS Appl. Mater. Interfaces* **2021**, *13*, 8700.
[21] Y.-S. Lan, X.-R. Chen, C.-E. Hu, Y. Cheng, Q.-F. Chen, *J. Mater. Chem. A* **2019**, *7*, 11134.
[22] Y. Shen, J. Sun, Y. Chen, D. Ni, T. Li, A. Yoshikawa, Y. Kawazoe, Q. Wang, *J. Mater. Chem. A* **2022**, *10*, 21356.
[23] M. Simoncelli, N. Marzari, F. Mauri, *Nat. Phys.* **2019**, *15*, 809.
[24] J. Sun, C. Zhang, Z. Yang, Y. Shen, M. Hu, Q. Wang, *ACS Appl. Mater. & Interfaces* **2022**, *14*, 11493.
[25] Y. Chen, C. Zhang, J. Sun, D. Ni, C. Zhang, Q. Wang, *Appl. Surf. Sci.* **2023**, *635*, 157718.
[26] C. Zhang, J. Sun, Y. Shen, C. Zhang, Q. Wang, A. Yoshikawa, Y. Kawazoe, P. Jena, *Small* **2023**, *19*, 2303295.
[27] C. Hou, Y. Shen, Q. Wang, Y. Kawazoe, P. Jena, *J. Mater. Chem. A* **2023**, *11*, 167.
[28] B. Chen, Q. Ruan, K. Peng, W. Wang, F. Xiao, W. Lei, X. Ming, *ACS Appl. Nano Mater.* **2024**,*7*, 11.
[29] G. A. Slack, *J. Phys. Chem. Solids* **1973**, *34*, 321.
[30] Y. Guo, C. Zhang, J. Zhou, Q. Wang, P. Jena, *Phys. Rev. Appl.* **2019**, *11*, 064063.
[31] L. Liu, H. L. Zhuang, *Comput. Mater. Sci.* **2019**, *166*, 105.
[32] Y. L.e Page, P. Saxe, *Phys. Rev. B* **2002**, *65*, 104104.
[33] J. S. Kang, M. Li, H. Wu, H. Nguyen, Y. Hu, *Science* **2018**, *361*, 575.
[34] F. Q. Wang, J. Yu, Q. Wang, Y. Kawazoe, P. Jena, *Carbon* **2016**, *105*, 424.
[35] H. Huang, W. Li, C. Hu, X. Fan, *J. Mat. Chem. C* **2023**, *11*, 9449.
[36] C. Zhang, J. Sun, Y. Shen, W. Kang, Q. Wang, *J. Phys. Chem. Lett.* **2022**, *13*, 5734.
[37] G. Kresse, J. Furthmüller, *Phys. Rev. B* **1996**, *54*, 11169.
[38] P. E. Blöchl, *Phys. Rev. B* **1994**, *50*, 17953.
[39] G. Kresse, D. Joubert, *Phys. Rev. B* **1999**, *59*, 1758.
[40] J. P. Perdew, K. Burke, M. Ernzerhof, *Phys. Rev. Lett.* **1996**, *77*, 3865.
[41] Y. Hu, C. Storey, *J. Optim. Theory Appl.* **1991**, *69*, 139.
[42] L. Isaeva, G. Barbalinardo, D. Donadio, S. Baroni, *Nat. Commun.* **2019**, *10*, 3853.
[43] M. Simoncelli, N. Marzari, F. Mauri, *Phys. Rev. X* **2022**, *12*, 041011.
[44] M. Omini, A. Sparavigna, *Physica B: Cond. Matter* **1995**, *212*, 101.
[45] Z. Han, X. Yang, W. Li, T. Feng, X. Ruan, *Comput. Phys. Commun.* **2022**, *270*, 108179.
[46] A. Togo, I. Tanaka, *Scr. Mater.* **2015**, *108*, 1.
[47] F. Eriksson, E. Fransson, P. Erhart, *Adv. Theory Simul.* **2019**, *2*, 1800184.
[48] X. Wu, V. Varshney, J. Lee, Y. Pang, A. K. Roy, T. Luo, *Chem. Phys. Lett.* **2017**, *669*, 233.
[49] Z. Sun, K. Yuan, X. Zhang, G. Qin, X. Gong, D. Tang, *Phys. Chem. Chem. Phys.* **2019**, *21*, 15647.
[50] R. Hanus, J. George, M. Wood, A. Bonkowski, Y. Cheng, D. L. Abernathy, M. E. Manley, G. Hautier, G. J. Snyder, R. P. Hermann, *Mater. Today Phys.* **2021**, *18*, 100344.